

MAPPING FIRE SCARS USING RADARSAT-2 POLARIMETRIC SAR DATA

David G. Goodenough<sup>1,2</sup>, Hao Chen<sup>1</sup>, Ashlin Richardson<sup>1,2</sup>, Shane Cloude<sup>3</sup>, Wen Hong<sup>4</sup>, Yang Li<sup>4</sup>

<sup>1</sup>Pacific Forestry Centre, Canadian Forest Service, Natural Resources Canada, Victoria, BC, Canada

<sup>2</sup>University of Victoria, Victoria, BC, Canada

<sup>3</sup>AEL Consultants, Edinburgh, Scotland, UK

<sup>4</sup>National Key Lab of Microwave Imaging Technology, Institute of Electronics, Chinese Academy of Sciences, Beijing, China

**Abstract.** Climate change is increasing the frequency and size of wild fire events in Canada’s forests. The size, distribution, and remoteness of boreal forest fire events make them a challenge to accurately monitor. Radarsat-2 is all weather radar technology and offers high spatial resolution, cross polarization, polarimetric capabilities and wide swath width. In this paper, Radarsat-2 fine quad-pol data were analyzed, utilizing the polarimetric phase information to map historical fire scars over two main study sites. The study demonstrated that historical fire scars, less than 10 years old and without strong topographic variation, had distinct polarimetric signatures with relatively higher quad-pol probabilities, leading to detection with low false alarm rates. By combining polarimetric decomposition and new classification approaches, fire scars were extracted: the resulting burned areas matched the true burned areas, according to GIS polygons from the provincial forest fire database. Our new K-Nearest Neighbors Graph Clustering classifier, unlike the classical Wishart scheme, does not depend on backscatter intensity; relies more on polarization information, and is more tolerant of topographic variations. These new approaches have revealed an exciting new application, mapping historical fire scars with polarimetric radar.

**Résumé.** La fréquence et la superficie des incendies des forêts canadiennes sont accrues par le changement climatique. La superficie, la distribution ainsi que l’éloignement des feux dans la forêt boréale complexifient leur surveillance efficace et précise. L’antenne radar de Radarsat-2 permet l’acquisition de données à haute résolution spatiale, à différentes polarisations, sur une large fauchée et sa bande C est très peu sensible aux conditions atmosphériques. Cet article présente les résultats d’analyse de données Radarsat-2 Quad-Pol fin, où la phase polarimétrique a permis de cartographier les cicatrices forestières résultant de feux historiques survenus sur deux sites d’étude. L’étude démontre que les cicatrices, datant de 10 ans et moins et situées dans une région à faible variations topographiques, présentent des signatures polarimétriques statistiquement distinctes conduisant à une détection efficace, avec un faible taux de fausses alarmes. Selon les polygones SIG de la base de données provinciale sur les feux de forêt, les cicatrices de feux forestiers extraites par télédétection correspondent aux vérités terrain lorsque l’on combine les extrants d’une décomposition polarimétrique de l’information avec une nouvelle approche de classification. Contrairement à la méthode classique de classification Wishart, notre nouvelle approche de classification, par regroupement graphique des K plus proches voisins, ne dépend pas de l’intensité de rétrodiffusion. Notre méthode exploite davantage l’information polarimétrique et elle est moins sensible aux variations topographiques. Ces nouvelles approches ont permis de révéler une nouvelle application excitante, soit la cartographie historique des cicatrices résultant d’incendies de forêt à l’aide de la polarimétrie radar.

Introduction

Canada is home to 10% of the world’s forests. Climate change in Canada’s boreal forests, particularly longer and drier summers, has resulted in increasingly frequent and large wild fire events. Such increases are expected to have the greatest effect upon western and central Canadian forests (Flannigan et al., 2005). Accounting of annual carbon emissions from these fire events and monitoring changes in Canada’s forests are important activities at Natural Resources Canada (NRCan). In 2004, NRCan initiated a joint project between the Canadian Forest Service (CFS) and the Canada Centre for Remote Sensing (CCRS) to create a system, The

Canadian Wildland Fire Information System (CWFIS), used to estimate direct carbon emissions from Canadian wild fires (de Groot et al., 2007). Accurate knowledge of burned areas is required to produce burned area estimates at the national level for post fire mapping. Currently, optical remote sensors, SPOT-VGT and Landsat, are used to map burned areas at low resolution (1 km) and high resolution (30m) respectively. A final burned-area output is used as an input to the National Forest Carbon Monitoring, Accounting and Reporting System (NFCMARS) (Kurz and Apps, 2006) to estimate national carbon emissions. However, for producing such burned area estimates, the earliest possible cloud-free satellite images are critical. Because of adverse weather, cloud and illumination conditions in the North, the limitations of remote sensing images from these optical sensors is evident.

Historic burned area estimates, created from sketch mapping from small planes, GPS mapping from helicopters, and photo interpretation (Fraser et al., 2004; Fraser et al., 2000), are also available from provincial and territorial forest fire agencies. Because the management and protection of these data resources fall under different provincial and territorial jurisdictions, GIS wild fire polygon data varies in quality due to the limitations of the traditional GIS technologies available at the time of mapping. Several Canadian provinces maintain GIS wild fire polygon data for managed forests from the 1940's to the present day. Generally, the older the data the less reliable it becomes. Fire perimeters derived from these traditional methods often include unburned "islands" and may overestimate burned areas. Moreover, the distribution of remote wild fire events and environmental conditions make them a challenge to accurately map.

Research has been conducted in mapping forest fire scars using Synthetic Aperture Radar (SAR), an all weather technology which can be used to provide measurements of post-fire ecosystem changes in forest structure, ground surface exposure and soil moisture patterns (Bourgeau-Chavez et al., 1997; Landry et al., 1995). In Bourgeau-Chavez's studies based on radar backscatter analysis, they demonstrated that fire scars were detectable in a range of boreal ecosystems across the globe using C-band SAR and showed that the length of viewing time of fire scars with ERS or Radarsat-1 data was between three and seven years in Alaska and Canada (Bourgeau-Chavez et al., 2002). Because this approach is a manual interpretation method based on the backscatter intensity, the accuracy of fire scar detection results were largely affected by human error, seasonal variations, topographic effects, and environmental conditions.

In recent years, advanced space-borne SAR systems have become available, such as the Japanese ALOS PALSAR, the German TerraSAR-X, and the Canadian Radarsat-2. Over previous sensors, these offer better spatial resolution, shorter revisiting times, cross polarization, polarimetric SAR capability, and all-weather data acquisition capability. Quadrature polarization (quad-pol) data provide opportunities to improve fire scar detection using spaceborne SAR with greater effectiveness and consistency. In previous studies, we discovered that, using airborne Convair 580 C-band quad-pol data, we were able to detect an historical fire scar, more than fifty years old, over our study site in Hinton, Alberta, (Goodenough et al., 2006). We also showed that with ALOS PALSAR L-band quad-pol data we were able to accurately separate a nine year old fire scar from other land cover types in the Keg River region, Alberta (Cloude et al., 2010). In this paper, we focused on the detection of two fire scars (one in the northeast of China, the other in northern Alberta) both roughly nine years of age, using Radarsat-2 C-band quad-pol data. The analysis is comprised of data preprocessing, data quality assessment, decomposition analysis, and classification methodologies. The aim of this approach is to provide new and automated fire-scar mapping methodologies from Radarsat-2 quad-pol data as an alternative to Landsat in support of CWFIS and NFCMARS.

## Study Sites and Data Sets

Two study areas were selected in this study. One is located in Ta-He, Heilongjiang, in the Northeast of China, near the border between China and Russia and was part of a joint project between Canada and China. The centre geo-coordinates are 52°26'N latitude and 125°32'E longitude. The study area is about 400km<sup>2</sup> and is relatively flat with an average elevation range of 420m above sea level and an average slope less than 15°. The forest stands in this region are dominated by Larch and White Birch. A wild forest fire occurred in September, 2001, burning and damaging more than half of the site (Yuan and Chu, 2008). The other study area is near the

1  
2  
3  
4  
5  
6  
7  
8  
9  
10  
11  
12  
13  
14  
15  
16  
17  
18  
19  
20  
21  
22  
23  
24  
25  
26  
27  
28  
29  
30  
31  
32  
33  
34  
35  
36  
37  
38  
39  
40  
41  
42  
43  
44  
45  
46  
47  
48  
49  
50  
51  
52  
53  
54  
55  
56  
57  
58  
59  
60

Keg River region in north Alberta, Canada. The centre geo-coordinates are 57°35'N latitude and 117°45'W longitude. The study area is about 900 km<sup>2</sup> and the elevation of the site ranges from 400 to 800m above sea level. This region is dominated by coniferous forest species, as shown in a forest landcover map of Canada produced by the Earth Observation for Sustainable Development (EOSD) of Forests (Wood et al., 2002). The Keg River area has a known extensive fire history with multiple fires in every decade since 1950. The latest wild forest fire in this region occurred in 2002 which burned approximately 4830 hectares.

Radarsat-2 is a C-band microwave imaging radar operating with a frequency of 5.405 GHz. The Radarsat-2 data product used in this study was acquired in the fine resolution quad-polarization (FQ) beam mode, obtained by operating the radar to alternately transmit horizontal and vertical polarizations, while simultaneously receiving both horizontal and vertical polarizations (Slade, 2009). The data were collected by MacDonald, Dettwiler and Associates (MDA) and were delivered to us through the Canada Centre for Remote Sensing (CCRS) in a Single Look Complex (SLC) file format. Two Radarsat-2 FQ19 images were collected over the Ta-He site on July 14 and October 18, 2009, with a look angle of ~39°. Fig. 1(a) and (b) show the two images in Pauli RGB (Lee and Pottier, 2009) for the July and October images, respectively. The other two FQ10 images were acquired over the Keg River site on July 2 and July 26, 2010, with a look angle of ~30°. Fig. 1(c) and (d) are the two Pauli images for the July 2 and 26 images respectively. All Radarsat-2 images have the dimension of 29 km (L) × 27 km (W). The most important parameters of these images are summarized in Table 1.

For ground reference, a high-resolution SPOT5 Level 1A image was acquired over the Ta-He study site with 10m spatial resolution multi-spectral channels and a 2.5m resolution panchromatic channel. This SPOT5 image was collected on July 27, 2006 and was cloud free. The multispectral (10m) channels were clustered by using unsupervised K-means classifier (Lee et al., 2004) with the fire scar and forested areas identified. The Alberta historical wild fire GIS polygons, representing 2000's collections based on fire years, were provided by the Government of Alberta. The fire scar polygon in the Keg River region, digitized from aerial photos in 2002, was extracted from this GIS dataset. These auxiliary data were used in conjunction with Google Earth maps and local field knowledge to verify the burned areas identified from the radar images.

**Data Preprocessing and Assessment of Polarimetric Information**

The processing techniques employed for forestry all require estimation of the average coherency matrix [T] for a pixel. All data sets provided were in SLC format. The first stage of processing was to employ multi-looking and averaging to reduce speckle. Two pieces of information were required to determine the parameters for multi-looking and averaging: firstly the pixel dimensions in the data, and secondly the resolution of the sensor (which is generally larger than the pixel size so there is some degree of oversampling). The Radarsat-2 pixel has dimensions 4.73m × 5.11m and resolution 5m × 9m (slant range by azimuth). Using the European Space Agency's PolSARpro, we employed multi-looking on the FQ data by 4 (azimuth) × 2 (range), yielding an intermediate product with around 3 or 4 equivalent looks, allowing the use of square windows for speckle filtering.

A box car filter with window size 5 × 5 was employed to generate a 4 × 4 covariance matrix (C4), which resulted in approximately 107 ENL (Equivalent Number of Looks). The C4 matrix was converted to a 4 × 4 coherency matrix (T4), from which the mean Faraday rotation for the scene was estimated and removed (Freeman, 2004). After the correction of the T4 matrix for Faraday rotation, a 3 × 3 coherency matrix (T3) was extracted from the T4 matrix. The HV channels of the T3 matrix were then corrected for signal-to-noise ratio (SNR) by applying the HV/VH coherence in Equation 1 (Cloude, 2009).

$$\gamma = \frac{|C_{23}|}{\sqrt{C_{22}}\sqrt{C_{33}}} \tag{1}$$

A reflection symmetry condition  $\langle S_{HH} S_{HV}^* \rangle = \langle S_{HV} S_{VV}^* \rangle = 0$  in T3 must be satisfied as it is a basic assumption for many commonly-used polarimetric SAR decomposition methods, including the Freeman-Durden three-component decomposition (Freeman and Durden, 1998), a popular decomposition method for landcover applications. Generally, the reflection asymmetry effect (Lee and Pottier, 2009) of longer wave SAR data is induced by non-flat surface structures, such as topography, branches and leaves. For the Radarsat-2 C-band SAR,

the short wavelength return is more sensitive to the vegetation canopy than rough surfaces beneath it. To perform compensation, a Polarization Orientation Angle (POA) shift is estimated according to Equation (2) and (3) (Lee et al., 2000; Lee et al., 2002):

$$\eta = \frac{1}{4} \left[ \tan^{-1} \left( \frac{-4 \operatorname{Re}(\langle \tilde{S}_{HH} - \tilde{S}_{VV} \rangle \tilde{S}_{HV}^*)}{-\langle |\tilde{S}_{HH} - \tilde{S}_{VV}|^2 \rangle + 4 \langle |\tilde{S}_{HV}|^2 \rangle} \right) + \pi \right], \quad (2)$$

$$\theta = \begin{cases} \eta, & \text{if } \eta \leq \pi/4 \\ \eta - \pi/2, & \text{if } \eta > \pi/4 \end{cases}, \quad (3)$$

where  $\theta$  is the POA shift, and  $\tilde{S}_{HH}$ ,  $\tilde{S}_{VV}$ , and  $\tilde{S}_{HV}$  are terms from the polarimetric SAR scattering matrix and  $\operatorname{Re}$  denotes real part. The reflection asymmetry effect is compensated by removing the effect of the POA shift from the coherency matrix T3 as in Equation (4) (Lee et al., 2000; Lee et al., 2002). The compensation algorithm does not use any other data sources, but depends solely upon the coherency matrix T3:

$$T^{\text{new}} = UTU^T, U = \begin{bmatrix} 1 & 0 & 0 \\ 0 & \cos 2\theta & \sin 2\theta \\ 0 & -\sin 2\theta & \cos 2\theta \end{bmatrix}. \quad (4)$$

Assessment of the overall quality of polarimetric SAR information present in the dataset was performed. We assessed the usefulness of using the quad-pol mode, above and beyond the simpler dual-pol polarimetric beam mode by examining a test statistic, the quad-pol probability shown in Equation (5), where  $\Delta\alpha$  is the differential alpha and  $\sigma$  is an entropy dependent scale parameter (Cloude, 2009). Fig. 2(a) and (b) are the quad-pol probability images generated from the same data sets over the Ta-He and Keg River respectively. The burned regions show relatively higher quad-pol probabilities, contrasted with the forest areas in lower probabilities. This suggests that the burned areas have a distinct polarimetric signature, which requires for characterization, the extra phase information in the quad-pol data (above and beyond the dual-pol information). Consequently, the quad-pol data is required for unambiguous characterization of burned areas.

$$p(\Delta\alpha) = \frac{\Delta\alpha}{\sigma^2} \exp\left(-\frac{\Delta\alpha^2}{2\sigma^2}\right) \quad (5)$$

Based on the quality assessment of the images, the July 14<sup>th</sup>, 2009 Ta-He image and the July 26<sup>th</sup>, 2010 Keg River images were not analyzed further, since firstly, higher entropies were observed over the burned areas in the HV/VH coherence images, indicating greater image homogeneity, and secondly, the quad-pol probability showed only a marginal advantage of the quad-pol information. Therefore, further analysis was performed on the quad-pol data collected from October 18<sup>th</sup>, 2009 over Ta-He and from July 4<sup>th</sup>, 2010 over Keg River.

## Polarimetric SAR Decompositions

Polarimetric SAR decompositions were performed on the calibrated T3 matrices for interpretation of the structural variations of different decomposition parameters and for preparation of fire scar classifications and extractions. Two commonly used decomposition methods considered in our study were the Cloude-Pottier Entropy-alpha decomposition and the Freeman-Durden three-component decomposition.

### Entropy-alpha decomposition

The Entropy-alpha decomposition (Cloude and Pottier, 1997) is based on the eigenvalue/eigenvector analysis of the coherence matrix T3 and expressed as Equation (6).

$$T = \lambda_1 (e_1 e_1^{*T}) + \lambda_2 (e_2 e_2^{*T}) + \lambda_3 (e_3 e_3^{*T}) \quad (6)$$

$$e_i = [\cos \alpha_i, \sin \alpha_i \cos \beta_i e^{i\delta_i}, \sin \alpha_i \sin \beta_i e^{i\gamma_i}]^T \quad (7)$$

$$H = -P_1 \log_2 P_1 - P_2 \log_2 P_2 - P_3 \log_2 P_3 \quad (8)$$

$$\alpha = P_1 \alpha_1 + P_2 \alpha_2 - P_3 \alpha_3 \quad (9)$$



$$A = \frac{\lambda_2 - \lambda_3}{\lambda_2 + \lambda_3} \quad (10)$$

where  $P_i = \frac{\lambda_i}{\lambda_1 + \lambda_2 + \lambda_3}$ ,  $\lambda_i$  are the corresponding eigenvalues,  $e_i$  are the corresponding eigenvectors (7), and  $i =$

1, 2, 3. The polarimetric scattering entropy  $H$  (8) measures randomness of scattering mechanisms. If  $H$  is 0, the scattering is deemed to be anisotropic. If  $H$  is 1, the scattering is deemed to be isotropic (random). The average  $\alpha$  angle is defined in Equation (9) and is employed for discriminating targets based upon the type of scattering mechanism. In particular, when  $\alpha$  is  $0^\circ$ , the mechanism is surface scattering. When  $\alpha$  is at  $45^\circ$ , it is dipole scattering. When  $\alpha$  is  $90^\circ$ , it is double bounce scattering.  $A$  is anisotropy (10), a normalized relation between the two minor eigenvalues. The anisotropy is also important for target discrimination, as it emphasizes the relative importance of secondary and tertiary scattering mechanisms.

Fig. 3(a) and (b) illustrate the corresponding entropy/ $\alpha$  distributions for the two sites, Ta-He and Keg River, respectively. Even though the structures shown in the entropy/ $\alpha$  planes are a little more compact for the two sites, there are components situated away from the lower bounding curve of the  $H/\alpha$  planes in both cases, indicating that the quad-pol data sets exhibit useful polarimetric information (Cloude, 2009).

### Three-component decomposition

The three-component decomposition (Freeman and Durden, 1998) decomposes total scattering power into surface, volume and double bounce components (11, 12).

$$T = m_v \begin{bmatrix} 2 & 0 & 0 \\ 0 & 1 & 0 \\ 0 & 0 & 1 \end{bmatrix} + m_s \begin{bmatrix} \cos^2 \alpha_s & \cos \alpha_s \sin \alpha_s e^{i\phi_s} & 0 \\ \cos \alpha_s \sin \alpha_s e^{-i\phi_s} & \sin^2 \alpha_s & 0 \\ 0 & 0 & 1 \end{bmatrix} + m_d \begin{bmatrix} \cos^2 \alpha_d & \cos \alpha_d \sin \alpha_d e^{i\phi_d} & 0 \\ \cos \alpha_d \sin \alpha_d e^{-i\phi_d} & \sin^2 \alpha_d & 0 \\ 0 & 0 & 1 \end{bmatrix} \quad (11)$$

$$P = P_s + P_d + P_v = m_s + m_d + 4m_v \quad (12)$$

Here,  $P_s$ ,  $P_d$ , and  $P_v$  are the power components in terms of surface, double bounce and volume scattering. This decomposition approach was useful for isolating different scattering environments in a forested area. Forests have strong volume scattering, whereas fire scars show relatively strong surface scattering with mixed volume and double bounce scattering. Both clear-cuts and exposed land show strong surface scattering. In the next section, we show how to apply these decomposition results to the second-stage classification for fire scar delineation and mapping.

Fig. 4(a) and (b) present the three component decomposition images over Ta-He and Keg River, respectively. Forested areas display strong volume scattering returns, appearing green in the decomposition images. Man-made objects show up very clearly in bright colors. Burned areas appear mixed grey and blue in the Ta-He image and dark blue in the Keg River image, contrasting clearly with the forest and other objects. As expected, we see very good diversity of polarimetric response across different land types in the decomposition images, indicating the importance of the Radarsat-2 quad-pol mode.

### Unsupervised Classification Techniques for Fire Scar Extraction

Polarization information revealed through the decomposition parameters showed great potential for using Radarsat-2 quad-pol data to measure different scattering characteristics. Several classification techniques were investigated to explore effective fire scar identification and extraction based on these scattering characteristics and two of them are described in this paper. One is the Freeman-Durden Wishart classification (Lee et al., 2004) and the other is our latest development, the K-Nearest Neighbors Graph Clustering (KGC) technique (Richardson et al., 2010).

### Freeman-Durden Wishart Classification

The Freeman-Durden Wishart Classification was first introduced by Lee (Lee et al., 2004). The Freeman-Durden's three-component decomposition places pixels in permanent categories according to the dominant scattering mechanism (as determined by the surface, volume and double bounce scattering power components of the Freeman-Durden decomposition). Once the polarimetric SAR data has been divided into three categories of pixels that are each dominated by the surface scattering mechanism, volume scattering mechanism and double bounce scattering mechanism, respectively, the categories are further subdivided, according to the magnitude of the dominant power given by the Freeman decomposition, into small initial clusters of approximately equal numbers of pixels, which are ordered in terms of the magnitude of the dominant power. These small initial clusters act as the initialization for the next step: an agglomerative merging, which is conducted based on the intra-cluster Wishart distance (13) (the agglomeration step is applied until a desired number of final clusters is reached).

$$D_{ij} = \frac{1}{2} \{ \ln(|V_i|) + \ln(|V_j|) + \text{Tr}(V_i^{-1}V_j + V_j^{-1}V_i) \} \quad (13)$$

In (13),  $V_i$  and  $V_j$  represent the coherency matrices that are representative of cluster  $i$  and cluster  $j$  respectively. The membership of the clusters is further optimized using the K-means iteration by means of the Wishart distance (14), whereby each pixel with covariance matrix  $Z$  is assigned to the nearest K-means cluster, according to the covariance matrix  $V_m$  representing that cluster.

$$d(Z, V_m) = \ln|V_m| + \text{Tr}(V_m^{-1}Z) \quad (14)$$

This optimization by K-means iteration continues until the number of pixels changing classes is below a predetermined threshold. Since the pixels in the three categories are kept separate from one another, the advantage of this unsupervised classification is to produce the classes that contain pixels with the same type of scattering mechanism.

### K-Nearest Neighbors Graph Clustering (KGC)

The K-Nearest Neighbors Graph Clustering (KGC) classifier has two stages. 1) We estimate the density value at each point in the feature space. 2) We climb the density estimate, elucidating arbitrarily shaped "modes" in the density; i.e., the modes are considered to be peaks in the density, as in (Wishart, 1969). The "hill climbing" is performed on the K-Nearest Neighbors (KNN) graph, a directed graph whose nodes correspond to the points of the feature space. From each node of the graph, "K" edges emanate, connecting the point with each of its "K" nearest neighbors. The density estimate at each point is computed using the "K" nearest neighbors – consequently, 1) and 2) are defined in a way that they are consistent with one another, ensuring that the scheme is both stable and deterministic with respect to initial conditions and the order of merging. The parameter "K" implicitly defines the number of classes so that the clusters are well formed - both in shape and in quantity - by the estimated density in the feature space.

A practical method (15) is estimating the density at a point  $x$  as the reciprocal of the average of the distances to the K-nearest neighbors of  $x$ :

$$\rho(x) = \frac{1}{\frac{1}{K} \sum_{n \in N} d(x, n)} \quad (15)$$

Here,  $N$  denotes the K-nearest neighbors of  $x$ , and  $n$  is an element of  $N$ . Note that increasing the value of "K" takes more information about a point into consideration. Setting  $K=1$ , the estimate is completely local, which will result in producing a high number of clusters. Larger values of  $K$  will yield increasingly global estimates, decreasing the granularity of the result, so that fewer clusters are produced.

After computing the K-nearest neighbors of each point, a KNN graph is constructed. Following the assignment of an estimated density to each node, we perform a "hill climb" on the graph, reaching the highest density points, which are then deemed representative elements of clusters. This is accomplished by a function visiting the graph's nodes recursively: an iteration of the function performed at each node. Upon visiting a node, if the node's density is greater than that of every K-neighbor, the iteration terminates, whereby the node is

1  
2  
3  
4  
5  
6  
7  
8  
9  
10  
11  
12  
13  
14  
15  
16  
17  
18  
19  
20  
21  
22  
23  
24  
25  
26  
27  
28  
29  
30  
31  
32  
33  
34  
35  
36  
37  
38  
39  
40  
41  
42  
43  
44  
45  
46  
47  
48  
49  
50  
51  
52  
53  
54  
55  
56  
57  
58  
59  
60

deemed to represent an “attractive center” of the data (and is given a new label). Else if the current node is already labeled - the iteration terminates (in either case, upon termination, all other nodes visited during that iteration are assigned the label of the final node). Otherwise the current node must have a neighbor of higher density – accordingly, we visit the highest density neighbor. At each subsequent visit, we consider again the above three possibilities. The “attractive center” together with all of the points “attracted” to it, through the activity of the recursive function, represent a cluster.

For the purpose of illustrating the KNN graph clustering algorithm, we exhibit a KNN graph in Fig. 5, in which, the data points are represented by the smaller spheres. Furthermore, the larger spheres represent data points that have been determined to be “attractive centres”. For this example, four clusters were found. The spheres are colored to indicate the cluster membership. The KNN technique was applied for the data in a three dimensional feature space: entropy, alpha (Cloude and Pottier, 1997), and Shannon Entropy (Réfrégier and Morio, 2006). The technique is also applicable to higher dimensional data, for which the operator may select any desired three dimensional combination for visualization.

The KGC classifier is data driven with only one required parameter  $K$ . It finds clusters of arbitrary shape among the points scattered throughout the feature space, without directly assuming any underlying parameterized distribution (e.g. Wishart) in the input data. Consequently a benefit of KGC is greater stability with respect to the initial conditions (in this case, the parameter  $K$ ) as the issues relating to the order of merging and the choice of initial segments do not apply to the hill-finding approach, as it is non-agglomerative.

**Results and Discussion**

The Wishart classification with the Freeman-Durden decomposition initialization was performed on the FQ19 data set (October 18, 2009) over the Ta-He site. For comparison, a K-means classification for the SPOT5 data is shown in Fig. 6(c). Three clusters were identified as: Forest (Green), Fire Scar (Blue), and Mixed (Red). Fig. 6(a) is a classification map from the FQ19 data with no reflection asymmetry compensation. Some of the burned areas were being grouped into the volume category, changing both the cluster merging and classification results and exaggerating the proportion of the volume scattering component. Fig. 6(b) is the classification map from the FQ19 data with reflection asymmetry compensation - here the importance of the reflection asymmetry compensation is seen. The initial number of ‘seed’ clusters in each category of the Wishart classification was set to 90. The termination criteria were set to: 1) the number of pixels switching classes was no more than 1% of the total pixel number of the image, and 2) the number of iterations was not greater than 12. To compare the radar classification results with the SPOT5 classification, we merged 15 clusters from the output of the Wishart classification with Freeman-Durden initialization into the three main classes. The accuracy assessment of the fire scars mapping was determined by comparing the classification image with the SPOT5 K-clustering classification map: 80% of the forested areas and 85% of the fire scar areas in the radar cluster image agreed with the SPOT5 classification image.

To illustrate the advantages of the new KGC classification over a topographically challenging region in Keg River, two algorithms were run for comparison. The first was the Lee’s Freeman-Durden Wishart classification featuring a permanent partition into three categories (Surface, Volume, Double bounce scattering) based on the dominant power given by the Freeman-Durden decomposition. It was interesting to note that Lee’s algorithm successfully produced the fire scar boundary, using a much greater quantity of initial segments (450 per category) than originally recommended by the authors (30 per category). Since few double bounce pixels were found (leaving only single and volume categories), the use of excessive initial segments somewhat manhandles the algorithm away from its intended function of “preserving scattering characteristics” towards a purely agglomerative scheme (which, in this case, seems arguably better prepared to handle clusters of unusual structure). The binary classification result is shown in Fig. 7(a). No additional filtering was used; 50 final classes were selected. Lee’s classification was shown to be unstable: by changing the number of classes to 40, the fire scar boundary was lost in confusion with both urban and natural areas.

Fig. 7(b) indicates the fire scar class resulting from the KGC methodology, which used the decomposition parameters,  $H$ ,  $\alpha$  and  $A$ , from the Cloude-Pottier decomposition in the three-dimensional feature space. Fig. 7(b) was produced using  $K=220$  and the density estimate shown in Equation (13) resulting in 63

classes. The fire scars map produced by KGC was compared with the Alberta historical wild fire GIS polygons in the Keg River region. 84% of the KGC fire scars pixels fell inside the perimeters of the GIS polygon, covering 59% of the GIS polygon area. The area of the GIS fire polygons was larger than the KGC fire scar area because the former treated every pixel inside the polygons as a burned pixel. Nevertheless, the latter considered some of those pixels inside the GIS polygons as the unburned islands. Both of the KGC output and the GIS polygon were loaded onto Google Earth to verify the burned areas, Fig. 7(c), and the excellent agreement obtained.

In this paper, Radarsat-2 data at fixed angle of incidence was presented (around  $39^\circ$  for Ta-He and  $30^\circ$  for Keg River). The scattering mechanisms change with angle of incidence, as does the entropy of rough surface scattering (the latter generally increasing with increasing angle). Given the flexibility of Radarsat 2 to provide quad-pol data at variable incidence angles, it is necessary for us to continue investigating how difference in incidence angle affects the fire scar classification and mapping and finding ones that may better suit the development of a robust fire scar detector than the angles used here. In the long term, Radarsat -2 quad-pol data from several angles of incidence could be combined to improve the overall accuracy of fire scar mapping.

## Conclusions

This paper focuses on utilizing the phase information contained in Radarsat-2 quad-pol data to increase the sensitivity of SAR measurement for scar detection and classification. Two Radarsat-2 FQ data sets were processed and analyzed over two study sites. The results showed that it is feasible to map historical fire scars of approximately 9 years of age with Radarsat-2 quad-pol data, in different forest environments. The unsupervised Wishart classification based on the Freeman-Durden decomposition was implemented and applied. Different options for the initial number of 'seed' clusters in each category of the Wishart classification were considered. The classification results indicated that the reflection asymmetry effect compensation was an important factor that would reduce topography effects and improve the classification accuracy. The classification results were found to agree, in general, with the reference SPOT5 data with 80% of the forested areas and 85% of the fire scar areas agreeing with the SPOT5 classification image.

The KGC classification results are encouraging, showing the effectiveness of the new methodology in segmenting and classifying polarimetric SAR data for fire scar detection. Compared to the Freeman-Durden Wishart classification (based on stricter statistical assumptions and more restrictive initializations) the KGC classifier demonstrated a superior ability to resolve clusters with non-linear shapes. Furthermore, the KGC algorithm provided a vehicle for testing the consistency of feature space initialization followed by matrix space optimization. Experiments addressing this issue using the appropriate vector and matrix distance functions are in progress. The validity of the results is being further evaluated using GIS ground reference data and other remote sensing data from a variety of sources.

Our study results demonstrated that extra information embedded in Radarsat-2 quad-pol provided better forest monitoring capabilities from space, especially for the fire scar identification and extraction. Historical fire scars older than 7 years are generally not detectable in Landsat TM and SPOT (Bourgeau-Chavez et al., 2002). Using polarimetric C-band SAR data, the results showed it is certainly possible to improve the mapping of historical fire scars in this age category. Earlier we had shown that L-band PALSAR data could be used to accurately map and determine the age of much older fire scars (Goodenough et al., 2010). With the methodologies we developed through our studies, multitemporal collection and automatic data processing for forest fire scar detection became feasible, which is complementary to optical remote sensing and current fire scar mapping techniques. Accurate information of area burned, age and frequency of fires, improves our knowledge of carbon emissions into the atmosphere from forest fires.

## Acknowledgements

The authors would like to acknowledge the financial support of Natural Resources Canada, the Canadian Space Agency (CSA), the Province of British Columbia, and the Ministry of Science and Technology of the People's Republic of China. We thank Dr. Jong-Sen Lee for providing valuable information on the implementation of the Freeman-Durden Wishart classification and Dr. Eric Pottier for his assistance with ESA



PolSARpro. We thank Dr. Francois Charbonneau for the translation of the abstract in French. We appreciate MDA, CSA and CCRS for providing Radarsat-2 quad-pol data.

References

Bourgeau-Chavez, L.L., Harrell, P.A., Kasischke, E.S., and French, N.H.F. 1997. The Detection and Mapping of Alaskan Wildfires Using a Apaceborne Imaging Radar system. *International Journal of Remote Sensing*, Vol. 18, pp. 355–373.

Bourgeau-Chavez, L.L., Kasischke, E. S., Brunzell, S., and Mudd, J. P. 2002. Mapping Fire Scars in Global Boreal Forests Using Imaging Radar Data. *International Journal of Remote Sensing*, Vol. 23, No. 20, pp. 4211–4234.

Cloude, S.R., and Pottier, E. 1997. An Entropy Based Classification Scheme for Land Applications of Polarimetric SAR. *IEEE Transactions on GeoScience and Remote Sensing*, Vol. 35, No. 1, pp. 68-78.

Cloude, S.R. 2009. *Polarisation: Applications in Remote Sensing*. Oxford New York, Oxford University Press, ISBN: 978-0-19-956973-1.

Cloude, S.R., Marino, A., Goodenough, D.G., Chen, H., Richardson, A., and Moa, B. 2010. Radar Polarimetry for Forestry Applications: ALOS and Radarsat-2 Studies in Canada. In *ForestSat 2010: Proceedings of ForestSat*, 7-9 September 2010, Lugo and Santiago de Compostela, Spain.

de Groot, W.J., Landry, R., Kurz, W.A., Anderson, K.R., Englefield, P., Fraser, R.H., Hall, R.J., Banfield, E., Raymond, D.A., Decker, V., Lynham, T.J., and Pritchard, J.M. 2007. Estimating direct carbon emissions from Canadian wildland fires. *International Journal of Wildland Fire*, Vol. 16, pp. 593–606.

Flannigan, M.D., Logan, K.A., Amiro, B.D., Skinner, W.R., and Stocks, B.J. 2005. Future Area Burned in Canada. *Climatic Change*, Vol. 72, pp. 1-16.

Fraser, R.H., Li, Z., and Cihlar, J. 2000. Hotspot and NDVI differencing synergy (HANDS): a new technique for burned area mapping over boreal forest. *Remote Sensing of Environment*, Vol. 74, pp. 362–376.

Fraser, R.H., Hall, R.J., Landry, R., Lynham, T.J., Lee, B.S., and Li, Z. 2004. Validation and Calibration of Canada-wide Coarse-resolution Satellite Burned Area Maps. *Photogrammetric Engineering and Remote Sensing*, Vol. 70, pp. 451–460.

Freeman, A., and Durden, S.L. 1998. A three-component scattering model for polarimetric SAR data. *IEEE Transactions on Geoscience and Remote Sensing*, Vol. 36, No. 3, pp. 936-973.

Freeman, A. 2004. Calibration of Linearly Polarized Polarimetric SAR Data Subject to Faraday Rotation. *IEEE Transactions on Geoscience and Remote Sensing*, Vol. 42, No. 8, pp. 1617-1624.

Goodenough, D.G., Chen, H., and Dyk A. 2006. Evaluation of Convair-580 and Simulated Radarsat-2 Polarimetric SAR for Forest Change Detection. In *IGARSS'06: Proceedings of the International Geoscience and Remote Sensing Symposium*, 31 July - 4 August 2006, Denver, IEEE, Colorado, USA.

Goodenough, D.G., Hong, W., Chen, H., Li, Y., Richardson, A., Cao, F., Chen, E., Wang, P., and Hobart, G. 2010. Mapping Fire Scars From Space Using Radarsat-2 Polarimetric SAR. In *ASTRO 2010: Proceedings of 15th CASI Astronautics Conference*, 4-6 May 2010, Toronto, Ontario.

Kurz, W.A., and Apps, M.J. 2006. Developing Canada's National Forest Carbon Monitoring, Accounting and Reporting System to Meet the Reporting Requirments of the KYOTO Protocol. *Mitigation and Adaptation Strategies for Global Change*, Vol. 11, pp. 33-43.

Landry, R., Ahern, F.J., and O'Neil, R. 1995. Forest burn visibility on C-HH radar images. *Canadian Journal of Remote Sensing*, Vol. 21, pp. 204–206.

Lee, J.S, Schuler, D.L., and Ainsworth, T.L. 2000. Polarimetric SAR data compensation for terrain azimuth slope correction. *IEEE Transactions on GeoScience and Remote Sensing*, Vol. 38, No. 5, pp. 2153-2163.

Lee, J.S, Schuler, D.L., Ainsworth, T.L., Krogager, E., Kasilingam, D., and Boerner, W.M. 2002. On the Estimation of Radar Polarization Orientation Shifts Induced by Terrain Slopes. *IEEE Transactions On Geoscience And Remote Sensing*, Vol. 40, No. 1, pp. 30-41.

Lee, J.S, Grunes, M.R., Pottier, E., and Ferro-Famil, L. 2004. Unsupervised Terrain Classification Preserving Polarimetric Scattering Characteristics. *IEEE Transactions on GeoScience and Remote Sensing*, Vol. 42, No. 4, pp. 722–731.

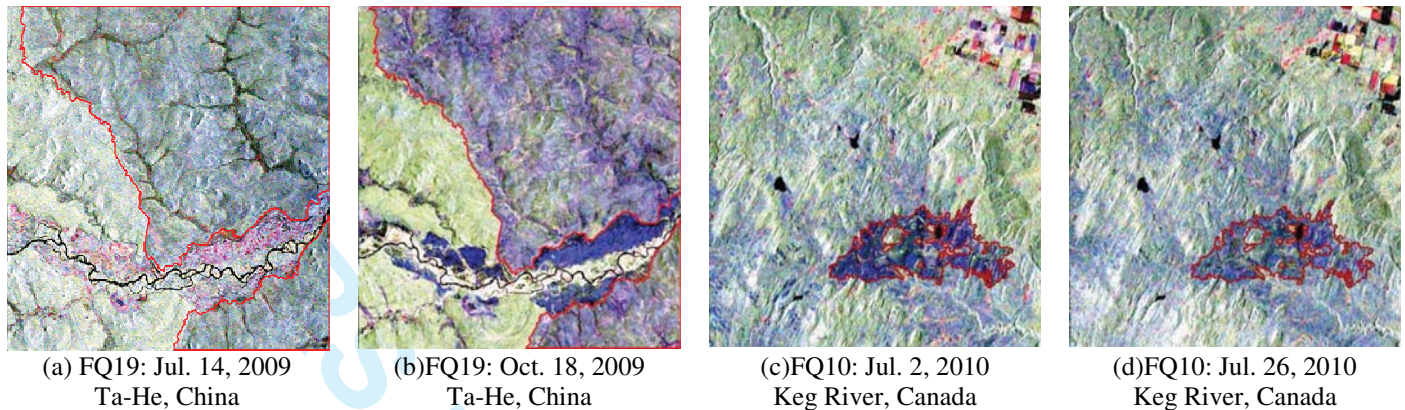
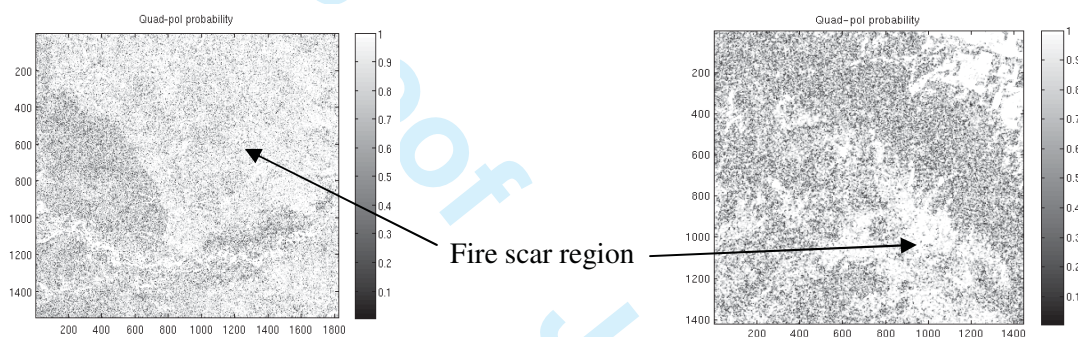
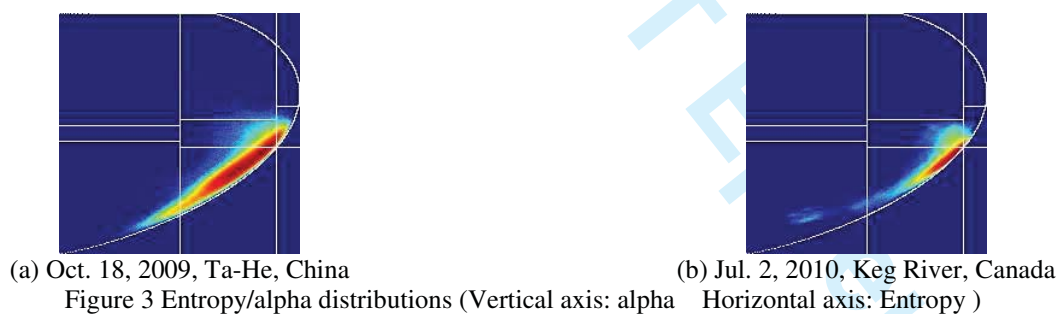
- 1  
2  
3 Lee, J.S, and Pottier, E. 2009. *Polarimetric Radar Imaging: from basics to applications*. CRC Press, Taylor &  
4 Francis Group, ISBN: 978-1-4200-5497-2.
- 5 Réfrégier, P. and Morio, J. 2006. Shannon entropy of partially polarized and partially coherent light with  
6 Gaussian fluctuations. *JOSA A*, Vol. 23, Issue 12, pp. 3036-3044.
- 7 Richardson, A., Goodenough D.G., Chen, H., Moa, B., Hobart, G., and Myrvold W. 2010. Unsupervised  
8 Nonparametric Classification of Polarimetric SAR Data Using the K-Nearest Neighbor Graph. In  
9 *IGARSS'10: Proceedings of the International Geoscience and Remote Sensing Symposium*, 25-30 July  
10 2010, Honolulu, IEEE, Hawaii, USA.
- 11 Slade, B. 2009. *Radarsat-2 Product Description*. MacDonald, Dettwiler and Associates, Vol. 1.
- 12 Wishart, D. 1969. *Mode Analysis: A Generalisation of Nearest Neighbour Which Reduces Chaining Effects*. In  
13 Numerical Taxonomy, ed. A.J. Cole, London: Academic Press.
- 14 Wood, J., Gillis, M.D., Goodenough, D.G., Hall, R.J., Leckie, D.G., Luther, J.E., and Wulder, M.A. 2002. Earth  
15 Observation for Sustainable Development of Forests (EOSD): Project Overview. In *IGARSS'02:*  
16 *Proceedings of the International Geoscience and Remote Sensing Symposium*, 24-26 June 2002, Toronto,  
17 IEE, Canada.
- 18 Yuan, G., and Chu, X. 2008. Current Condition and Features of Forest Resources at the 18th Forest Bureau.  
19 *Inner Mongolia Forestry Investigation Design*, Vol. 31, No. 2, PP. 55.
- 20  
21  
22  
23  
24  
25  
26  
27  
28  
29  
30  
31  
32  
33  
34  
35  
36  
37  
38  
39  
40  
41  
42  
43  
44  
45  
46  
47  
48  
49  
50  
51  
52  
53  
54  
55  
56  
57  
58  
59  
60

List of Tables

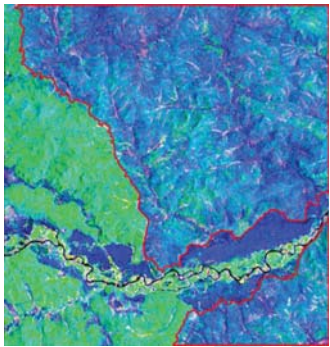
Table 1 Radarsat-2 image parameters

Acquisition date	July 14, 2009	October 18, 2009	July 4, 2010	July 26, 2010
Coverage	Ta-He, Heilongjiang, China		Keg River, AB, Canada	
Beam mode	Find Quad-pol 19		Find Quad-pol 10	
Orbital direction	Descending		Ascending	
Nominal swath	25km			
Pixel spacing	4.73m × 5.11m			
Spatial resolution	5m × 9m			
Angle of incidence	39°		30°	

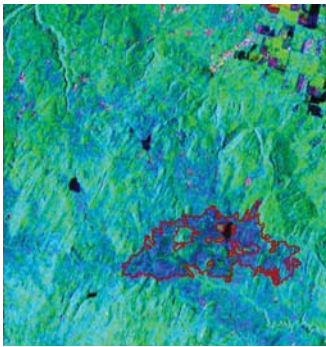
## List of Figures

Figure 1 Pauli RGB images of Radarsat-2 quad-pol data (Imagery dimension: 29 km  $\times$  27 km.)Figure 2 Quad-pol probabilities of Radarsat-2 quad-pol data (Imagery dimension: 29 km  $\times$  27 km)





(a) Oct. 18, 2009, Ta-He, China



(b) Jul. 2, 2010, Keg River, Canada

Figure 4 Freeman-Duden decomposition images.

R: Double bounce, G: Volume scattering, B: Rough surface  
(Imagery dimension: 29 km × 27 km)

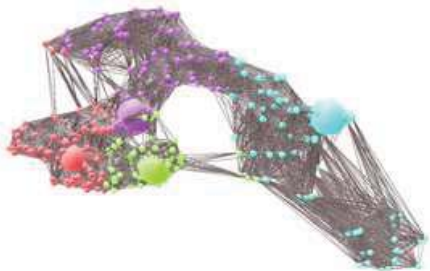
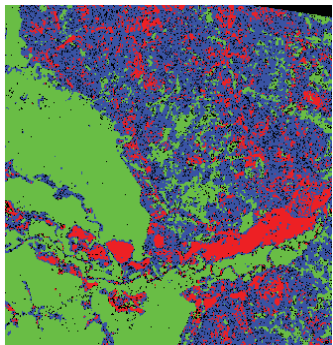
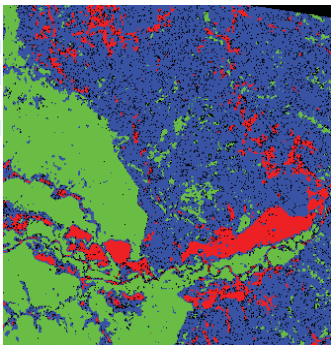


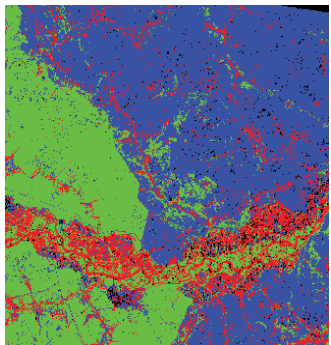
Figure 5 Illustration of a KNN clustering graph with K=40 in a three dimensional view



(a) Classification map without reflection asymmetry compensation

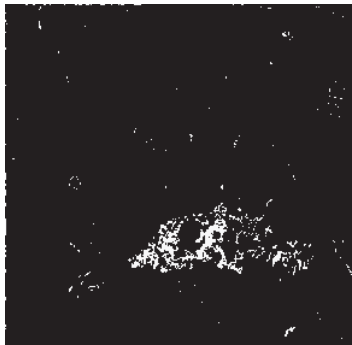


(b) Classification map with reflection asymmetry compensation



(c) K-means classification image of SPOT5

Figure 6 Radarsat-2 Wishart classifications with Freeman-Durden decomposition initialization (Oct. 18, 2009, Ta-He, China)  
R: Mixed G: Forest B: Fire Scar (Imagery dimension: 29 km × 27 km.)



(a) Fire scar retrieved from Freeman-Durden Wishart classification



(b) Fire scar retrieved from KGC classification



(c) KGC fire scar on Google Earth with GIS fire scar perimeters

Figure 7 2002 Fire scar identified from Radarsat-2 classifications (Jul. 2, 2010, Keg River, Canada)  
(Imagery dimension: 29 km × 27 km.)